

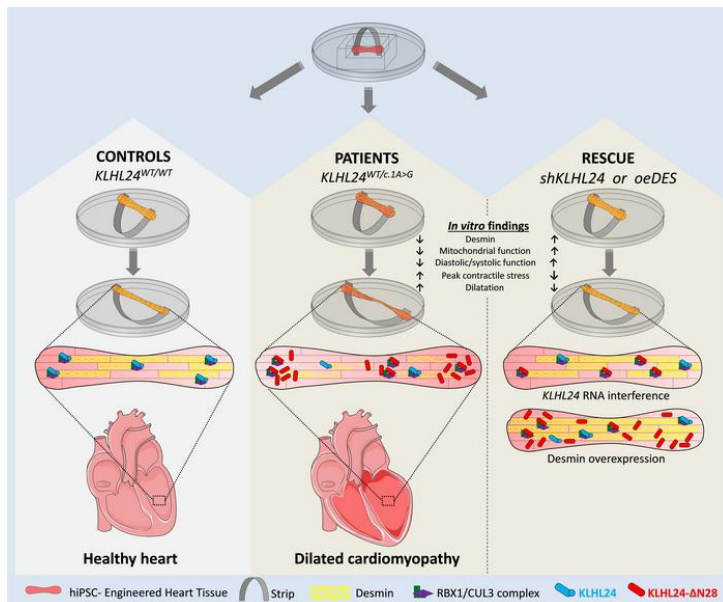
Gain-of-function mutation in ubiquitin-ligase KLHL24 causes desmin degradation and dilatation in hiPSC-derived engineered heart tissues

Mathilde C.S.C. Vermeer, ... , Herman H. W. Silljé, Peter van der Meer

J Clin Invest. 2021. <https://doi.org/10.1172/JCI140615>.

Research In-Press Preview Cardiology

Graphical abstract



Find the latest version:

<https://jci.me/140615/pdf>



Gain-of-function mutation in ubiquitin-ligase KLHL24 causes desmin degradation and dilatation in hiPSC-derived engineered heart tissues

Mathilde C.S.C. Vermeer¹, Maria C. Bolling^{2#}, Jacqueline M. Bliley^{4#}, Karla Arevalo Gomez¹, Mario Pavez-Giani¹, Duco Kramer², Pedro H. Romero-Herrera¹, B. Daan Westenbrink¹, Gilles F.H. Diercks³, Maarten P. van den Berg¹, Adam W. Feinberg⁴, Herman H.W. Silljé¹, Peter van der Meer^{1*}

¹*Department of Cardiology, University of Groningen, University Medical Center Groningen, Groningen, The Netherlands.* ²*Department of Dermatology, University of Groningen, University Medical Center Groningen, Groningen, The Netherlands.* ³*Department of Pathology, University Medical Center Groningen, University of Groningen, Groningen, The Netherlands.* ⁴*Department of Biomedical Engineering, Department of Materials Science & Engineering, Carnegie Mellon University, Pittsburgh, Pennsylvania, USA*

These authors contributed equally.

*Corresponding author: Department of Cardiology, University of Groningen, University Medical Center Groningen, Groningen, The Netherlands. Phone +31 503610671; E-mail: p.van.der.meer@umcg.nl

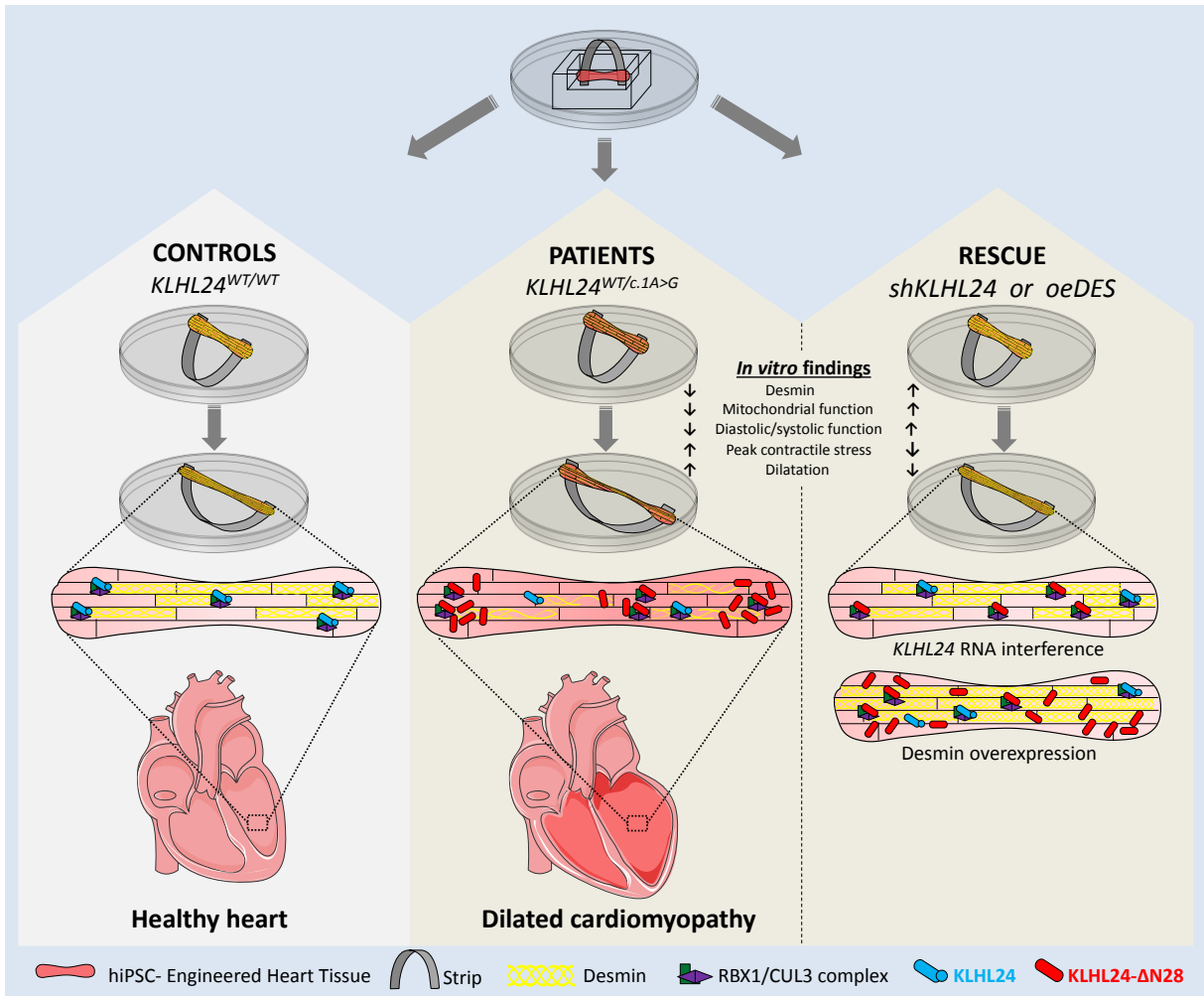
Conflict of interest statement: “The authors have declared that no conflict of interest exists”

1 **ABSTRACT**

2 The start codon c.1A>G mutation in *KLHL24*, encoding ubiquitin-ligase KLHL24, results in the loss of 28 N-
3 terminal amino acids (KLHL24-ΔN28) by skipping the initial start codon. In skin, KLHL24-ΔN28 leads to gain
4 of function, excessively targeting intermediate filament keratin-14 for proteasomal degradation, ultimately
5 causing epidermolysis bullosa simplex (EBS). The majority of these EBS-patients are also diagnosed with
6 dilated cardiomyopathy (DCM), but the pathological mechanism in the heart is unknown. As desmin is the
7 cardiac homologue of keratin-14, we hypothesized that KLHL24-ΔN28 leads to excessive degradation of
8 desmin, resulting in DCM. Dynamically loaded engineered heart tissues (dyn-EHTs) were generated from
9 human induced pluripotent stem cell (hiPSC)-derived cardiomyocytes from two patients and three (non)familial
10 controls. Ten-fold lower desmin protein levels were observed in patient-derived dyn-EHTs, in line with
11 diminished desmin levels detected in patients' explanted heart. This was accompanied by tissue dilatation,
12 impaired mitochondrial function, decreased force values and increased cardiomyocyte stress. HEK293
13 transfection studies confirmed KLHL24-mediated desmin degradation. *KLHL24* RNA interference or direct
14 desmin overexpression recovered desmin protein levels, restoring morphology and function in patient-derived
15 dyn-EHTs. To conclude, presence of KLHL24-ΔN28 in cardiomyocytes leads to excessive degradation of
16 desmin, affecting tissue morphology and function, that can be prevented by restoring desmin protein levels.

1 GRAPHICAL ABSTRACT

2



3
4

1 INTRODUCTION

2 Inherited cardiomyopathies are prevalent diseases with many cases of unknown etiology. New causative genes
3 are frequently discovered. We recently were the first to report a link between the heterozygous gain of function
4 *KLHL24:c.1A>G* mutation (Met1Val) causing epidermolysis bullosa simplex (EBS) in skin and dilated
5 cardiomyopathy (DCM) of the heart (1). Following our initial observation, around 33 patients with similar gain
6 of function mutations leading to DCM have been reported (2, 3). Despite these publications, the causative effects
7 of gain of function mutations in *KLHL24* leading to cardiomyopathy have not yet been established.

8 The *KLHL24:c.1A>G* mutation is one of the five described methionine start codon mutations (e.g.:
9 *c.1A>G*; *c.1A>T*; *c.2T>C*; *c.3G>A* and *c.3G>T*) in ubiquitin-ligase *KLHL24*, resulting in the loss of 28 N-
10 terminal amino acids (*KLHL24-ΔN28*) by skipping the initial start codon. In skin, it has been shown that
11 *KLHL24* functions as an ubiquitin-ligase, forming a protein complex with *CUL3* and *RBX1* that mediates
12 keratin 14 degradation. This process is tightly balanced through *KLHL24* auto-ubiquitination. In contrast, the
13 mutated protein *KLHL24-ΔN28* is unable to undergo auto-ubiquitination and is consequently more stable. This
14 results in excessive ubiquitination and therefore degradation of keratin 14, ultimately leading to skin fragility (4–
15 7).

16 Keratins (*KRT*) belong to the protein family of intermediate filaments (IFs) and are essential for the
17 keratinocyte cytoskeletal network in the skin. IFs provide cells with compliance to small deformations and,
18 simultaneously strengthen cells when subjected to stretch (8). Mutations in genes encoding different IFs have
19 been associated with EBS and inherited cardiomyopathies, as they serve major regulatory roles in stretch-bearing
20 tissues, like skin and heart (9, 10). Desmin (*DES*) is the essential IF in cardiomyocytes and skeletal muscle cells
21 (11). Desmin filaments extend the z-discs from one myofibril to another, forming a supportive latticework that
22 stretches all the way from the sarcolemma to the nuclear envelope. They position, stabilize and facilitate sensing
23 and transferring of signals between nucleus, cell membrane, mitochondria and myofibrils(12). When the IF
24 network in the heart is compromised, mitochondrial dysfunction becomes one of the earliest and most prominent
25 defects(10). Additionally, collapse of the desmin network results in nuclear delamination and intercalated disc
26 abnormalities, which ultimately leads to loss of cardiac function. Indeed, many *DES* mutations, and mutations in
27 other genes affecting the desmin network, have been implicated in these so-called desminopathies (10, 12–14).

28 Because desmin belongs to the same highly conserved family of intermediate filament proteins as
29 keratins (15), we hypothesized that *KLHL24-ΔN28* leads to excessive degradation of desmin in the heart,
30 causing DCM. To investigate this, we used human induced pluripotent stem cells (hiPSC) for the differentiation

1 of patient-specific *KLHL24*^{WT/c.1A>G} cardiomyocytes. To study the function of KLHL24 on cardiac tissue
2 compliance (i.e.: challenging the desmin network by stretch), a dynamically loaded engineered heart tissue (dyn-
3 EHT) model was employed (16). Here, a polydimethylsiloxane (PDMS) strip is attached to engineered heart
4 tissues (EHT) to simulate the loading (preload and afterload) experienced by the heart and bending of the strip
5 can be used to determine tissue contractile force via finite element modeling (FEM). This system can also be
6 dynamically cultured allowing to observe the morphological and functional changes that occur during ventricular
7 dilatation, which has been essential in revealing a clinically relevant phenotype in desmoplakin-mutated hiPSC-
8 CMs (16). In the current study, we show that a gain of function mutation in *KLHL24*, leading to KLHL24-ΔN28,
9 in cardiomyocytes results in excessive degradation of desmin, negatively impacting the morphology and function
10 of dyn-EHTs, can be prevented by *KLHL24* RNA interference or direct desmin overexpression.

1 RESULTS

2 Familial cases of Epidermolysis Bullosa Simplex with Dilated Cardiomyopathy

3 For this study, two patients of Dutch ancestry were included, both carriers of the *KLHL24*:c.1A>G mutation (1).
4 (Figure 1A; II:3 and III:2). This mutation leads to a truncated KLHL24 protein, KLHL24-ΔN28 (Figure 1B).
5 Both patients had typical aplasia cutis congenita and skin fragility, diagnosed as EBS, that improved over time.
6 In addition, the index patient (II:3) was diagnosed with a fast-progressive form of DCM at the age of 17, for
7 which he received a heart transplantation at the age of 18. His son (III:2), currently 18 years of age, is still
8 asymptomatic but his echocardiogram shows definite signs of DCM, characterized by left ventricular (LV)
9 dilatation, reduced LV ejection fraction (LVEF) and impaired global longitudinal systolic strain (Figure 1C-D).

10 Reduced desmin expression in the explanted heart and the generation of 3D cardiac tissues with the use of 11 hiPSC-derived cardiomyocytes

12 In the explanted heart of patient II:3, immunofluorescence analysis (IFA) revealed a lower desmin intensity than
13 was observed in other diseased heart explants, including idiopathic DCM, arrhythmogenic cardiomyopathy,
14 myocarditis and ischemic heart failure (Figure 2A and Supplemental Figure 1). Furthermore, structure of the
15 intracellular desmin network appeared intact and no desmin positive aggregates were observed in the explanted
16 heart of patient II:3. hiPSCs of the two patients in addition to one familial (I:1) and two non-familial healthy
17 controls were generated and validated (Supplemental Figure 2A-B). Localization of KLHL24 by IFA was
18 performed in hiPSC-derived control cardiomyocytes (hiPSC-CMs) cultured in 2D, where KLHL24 abundantly
19 localized at the intersection of desmin with desmosomes (Figure 2B and Supplemental Figure 2C).

20 To study the function of KLHL24 on cardiac tissue compliance, the dyn-EHT model was employed (see
21 graphical abstract) using PDMS strips of two different thickness' (i.e. 130 or 260 μm) resulting in an
22 approximate 8-fold difference in loading (16). Strikingly, culture of control-derived EHTs together with high
23 loading (dyn-EHTs, 260 μm thick strips) resulted in elevated mRNA expression of *KLHL24* and *DES*, compared
24 to dyn-EHTs with low loading using 130 μm thick strips (Supplemental Figure 2D). Given this elevated
25 expression in dyn-EHTs exposed to high loading, all further studies using patient and control-derived hiPSC-
26 CMs tissues were performed with 260 μm PDMS strips. Briefly, all EHTs were kept isometric constrained in the
27 well until day 14 to allow tissue formation (Supplemental Movie 1), and dynamically loaded (dyn-EHTs) from

1 day 14 (Supplemental Movie 2, control) till day 28 (Supplemental Movie 3, control) by removing the strip from
2 its physically constrained environment.

3 **Desmin is 10-fold reduced and affects morphology and function in patient-derived dyn-EHTs**

4 Morphologically, (Supplemental Movie 4-7 and Figure 2C) during dynamic loading, patient-derived dyn-EHTs
5 increased an additional 20% in diastolic length (11.6 ± 0.3 vs. 9.5 ± 0.3 mm; $p<0.0001$) compared to control
6 (Figure 2D). As a measure of tissue uniformity, we divided the smallest by the largest cross-sectional area of
7 tissues at baseline day 14 and 28. Control-derived tissues had a tissue uniformity ratio of 0.81 ± 0.03 suggesting a
8 relatively uniform tissue cross-sectional area along their length, whereas patient-derived tissues displayed a ratio
9 of 0.49 ± 0.05 ($p<0.0001$), indicating presence of very thin sections of tissue flanked by thicker sections (Figure
10 2D). IFA results in patient-derived dyn-EHTs showed that desmin was able to form normal IF networks (10),
11 similar to control networks, but the intensity of the desmin signal was highly reduced (Figure 2E and
12 Supplemental Figure 3). Quantification of immune-blotting revealed that desmin protein levels were 10-fold
13 lower in patient-derived dyn-EHTs compared to control ($p<0.001$), while mRNA levels remained unaffected
14 (Figure 2F and Supplemental Figure 4A-C). The protein levels of desmin's binding partners $\alpha\beta$ -crystallin, plectin
15 and desmoplakin, were not altered in dyn-EHTs. Whereas, actin, lamin A and C were increased ($p<0.05$), which
16 could be indicative of an adaptation to prevent nuclear delamination. Furthermore, phosphorylated GSK3 β ,
17 associated with cardiomyopathy and desmin disassembly (17), was significantly increased in patient-derived
18 dyn-EHTs (Figure 2F and Supplemental Figure 4B-C). On ultrastructure, transmission electron microscopy
19 (TEM) results showed more swollen-like mitochondria and electron denser glycogen storage vesicles in patient
20 compared to control-derived dyn-EHTs (Figure 2G). TEM also indicated that intercalated discs and myofibrils of
21 patient-derived tissues were similar to control at day 28 (Supplemental Figure 4D).

22 No differences in functional parameters were observed between patient and control-derived EHTs when
23 exposed to elevated loading upon initial onset of dynamic culture at day 14 (Figure 3; day 14). However, after 14
24 days of dynamic loading, striking differences were observed, suggesting that exposure to higher levels of loading
25 and increased culture time are needed to observe the changes between patient and control-derived tissues
26 (Supplemental Movie 5,7) First, dramatic differences in diastolic tissue stress were observed along the length of
27 patient-derived dyn-EHTs, with clear stress concentrations at the regions with decreased thickness. In contrast, a
28 more uniform diastolic tissue stress was observed in control-derived dyn-EHTs (Figure 3A; day 28). The peak
29 contractile stress was in fact 6-fold higher in patient-derived dyn-EHTs ($p<0.001$), which occurred because of

1 the reduced cross-sectional area, even though the contractile force was similar to control (Figure 3B). Patient-
2 derived dyn-EHTs furthermore displayed significantly decreased systolic force (0.67 ± 0.01 vs. 0.76 ± 0.02 mN;
3 $p<0.001$), but due to their reduced cross-sectional area, corresponding peak systolic stress levels were 3-fold
4 higher compared to control ($p<0.0001$). The same observation was seen in diastolic force (0.61 ± 0.02 vs.
5 0.72 ± 0.02 mN; $p<0.0001$) and corresponding peak diastolic stress ($p<0.0001$) (Figure 3C). Furthermore, the
6 average fractional shortening during dynamic loading increased up to considerable levels (20%) in control as
7 well as patient-derived dyn-EHTs (Figure 3D), in agreement with the overall intact myofibril ultrastructure.
8 Similarly to the observed differences in tissue stress and uniformity, regional fractional shortening varied widely
9 along the length of patient-derived dyn-EHTs, whereas, control-derived dyn-EHTs were quite uniform (Figure
10 3D-E). These results suggest that patient-derived tissues develop non-uniform contractile activity upon exposure
11 to dynamic loading.

12 **Gain of function ubiquitin-ligase KLHL24-ΔN28 targets desmin for excessive proteasomal degradation**

13 Desmin is a substrate for many different forms of post-translational modifications. Most of these lead to
14 disassembly of filamentous desmin, but only ubiquitination leads to desmin degradation (18). First, we
15 investigated high molecular weight (HMW) desmin bands in control and patient-derived dyn-EHTs, using an
16 antibody raised against the c-terminal epitope of desmin (clone Y66) that is unlikely to be masked by
17 ubiquitinated site-chains. As expected, the 52 kDa desmin band was highly reduced in patient-derived dyn-
18 EHTs, while an increase was observed in HMW-desmin bands, indicative for desmin ubiquitination (Figure 4A).
19 Quantification revealed a 2.3-fold elevation of HMW-desmin bands in patient compared to control-derived dyn-
20 EHTs ($p<0.001$) and the ratio of HMW-desmin/desmin was 15-fold higher in patient-derived dyn-EHTs
21 ($p<0.001$) (Supplemental Figure 5A). Second, by immunoprecipitation of desmin, we investigated direct
22 ubiquitinated levels in hiPSC-CMs, which demonstrated an increase of ubiquitinated desmin in patient-derived
23 extracts (Figure 4B). Transfection studies were furthermore performed to substantiate specific targeting of
24 desmin by the KLHL24/RBX1/CUL3(4)-ubiquitin ligase complex. In HEK293A cells, no endogenous desmin or
25 KLHL24, could be observed (Figure 4C). Transfection of cells with either desmin or KLHL24 plasmids
26 successfully resulted in detection of exogenous protein. To study the impact of wild type and truncated
27 (KLHL24-ΔN28) KLHL24 proteins on desmin levels, we performed equal ratio co-transfections using desmin,
28 ubiquitin-ligase factors RBX1 and CUL3 in either the presence or absence of KLHL24 or KLHL24-ΔN28
29 plasmids. Co-expression with KLHL24-ΔN28 resulted in a strong reduction in desmin protein levels. This effect

1 was also pronounced when wild type KLHL24 was co-expressed, while absent when a catalytically inactivate
2 form of KLHL24-ΔN28 was co-expressed (Figure 4C-D and Supplemental Figure 5B-C). Proteasomal
3 inhibition, via bortezomib treatment, furthermore prevented the ubiquitination-induced subsequent desmin
4 degradation, as shown on immune-blot (Figure 4E). As the expression of KLHL24 seems too excessive, we
5 adjusted the desmin:KLHL24 transfection ratio from 1:1 to 5:1, in order to observe the difference in desmin
6 ubiquitination between wild type and mutant KLHL24. After performing immunoprecipitation of flag-tagged
7 desmin, we indeed observed the strongest expression of ubiquitinated desmin in the KLHL24-ΔN28 group, like
8 in hiPSC-CMs (Supplemental Figure 5D). Based on these results, we have shown that loss of the first 28 amino
9 acids of the KLHL24 protein indeed leads to a more stable and therefore more abundant KLHL24 protein that
10 ubiquinates desmin excessively.

11 **Restoration of desmin protein levels rescues DCM phenotype in patient-derived dyn-EHTs**

12 To investigate if *KLHL24* RNAi would restore desmin protein levels in patient-derived hiPSC-CMs, we
13 generated short hairpin-mediated non-targeted (shNT) and *KLHL24* (shKLHL24) mRNA knockdown hiPSC
14 lines, using lentiviral constructs (Supplemental Figure 6A). To prove that desmin is a major contributor to the
15 phenotype, we additionally generated patient hiPSC lines with a desmin overexpression construct (oeDES)
16 (Supplemental Figure 6A). These lines were subsequently used for differentiation and generation of dyn-EHTs
17 (Figure 5A and Supplemental Movies 8-10). Both desmin overexpression and shKLHL24 resulted in a 3- to 7-
18 fold increase in desmin protein levels, respectively ($p < 0.01$) (Figure 5B and Supplemental Figure 6B-C). The
19 excessive tissue thinning observed in patients-derived dyn-EHTs was absent in shKLHL24 and oeDES tissues
20 ($p < 0.0001$). In addition, both rescue models prevented (most of) the dilatation (10.4 ± 0.3 in shKLHL24 and
21 9.0 ± 0.2 in oeDES vs. 11.5 ± 0.2 in shNT ($p < 0.05$); with respect to 9.5 ± 0.3 mm in control ($p = ns$)). As a result,
22 both the diastolic force (0.71 ± 0.01 in shKLHL24 and 0.70 ± 0.01 in oeDES vs. 0.61 ± 0.02 in shNT ($p < 0.01$); with
23 respect to 0.72 ± 0.02 mN in control ($p = ns$)) and systolic force restored (0.76 ± 0.02 in shKLHL24 and 0.74 ± 0.01
24 in oeDES vs. 0.66 ± 0.01 in shNT ($p < 0.05$); with respect to 0.76 ± 0.02 mN in control ($p = ns$)), fully returning the
25 peak diastolic ($p < 0.01$) and systolic stress ($p < 0.001$) to values observed in control-derived dyn-EHTs ($p = ns$)
26 (Figure 5C). This also resulted in restored peak contractile stress ($p < 0.05$) and normal variation in regional tissue
27 diastolic stress in patient-derived dyn-EHTs containing *KLHL24* RNAi or desmin overexpression, similar to
28 control-derived dyn-EHTs (Figure 5D,E).

1 As the mitochondrial morphology was impaired and electron density of glycogen granules was
2 increased in patient-derived dyn-EHTs, we investigated metabolic markers. On blot, shKLHL24 dyn-EHTs in
3 fact showed higher protein levels of oxidative phosphorylation complex III and IV compared to shNT patient-
4 derived dyn-EHTs ($p < 0.01$). Whereas, these levels also normalized in oeDES dyn-EHTs (Figure 5F and
5 Supplemental Figure 6D). Direct measurements of glycolytic acidification and oxygen consumption rates of
6 hiPSC-CMs corroborated these findings, showing normal basal ($p < 0.05$) and maximal respiratory capacities
7 ($p < 0.01$) after rescue, during mitochondrial stress-testing (Supplemental Figure 7). Meanwhile in tissues, *PDK4*
8 mRNA expression increased ($p < 0.05$) in both shKLHL24 and oeDES patient-derived dyn-EHTs, while *HADHB*
9 expression also increased in oeDES dyn-EHTs ($p < 0.001$). On the other hand, *GLUT4* expression decreased in
10 both rescue groups ($p < 0.05$), compared to both control and non-rescued patient-derived dyn-EHTs
11 (Supplemental Figure 8). These data suggest that restoration of desmin protein levels enhances beta-oxidation
12 while preventing excessive glucose utilization, as is normal for cardiac muscle.

1 DISCUSSION

2 A cardio-cutaneous syndrome is a devastating, rare inheritable disease that affects both the skin and heart (19).
3 In the current study, we explored a novel gene causative of a cardio-cutaneous syndrome, called *KLHL24* (1, 2).
4 We demonstrate with the use of 3D cardiac tissue engineering, that a gain of function mutation in *KLHL24* leads
5 to excessive proteasomal degradation of desmin. This results in tissue dilatation, reduced contractile force,
6 increased stress and impaired mitochondrial function. With the use of RNAi of *KLHL24* or overexpression of
7 desmin, the morphology and function could be rescued. These results make *KLHL24* RNAi a well suited
8 potential therapeutic strategy applicable for patients suffering from this genetic disorder.

9 A cardio-cutaneous syndrome is caused by dominant or recessive mutations, mostly in genes encoding
10 for two desmosomal proteins, namely desmoplakin and plakoglobin (20). Both proteins are incorporated into
11 cell-cell connecting structures called desmosomes and both are commonly shared by cardiac and cutaneous
12 tissues (21). Desmosomes are also known for their intracellular anchorage of the IF network. In that sense,
13 *KLHL24* appears to be the first protein that regulates the turnover of both IF types, namely keratins and desmin.
14 In our dyn-EHTs, we observed a difference of 15-fold in the protein ratio of desmin versus HMW-desmin. Using
15 immunoprecipitation of desmin, we in fact showed more ubiquitinated desmin in patient-derived hiPSC-CMs. In
16 addition to the 10-fold reduced functional desmin protein levels found in patient-derived cardiac tissues, our co-
17 transfection studies substantiated the ability of *KLHL24* and *KLHL24-ΔN28* to degrade desmin through
18 ubiquitination and proteosomal degradation. Overexpression of *KLHL24* and *KLHL24-ΔN28* in HEK cells
19 clearly resulted in detectable protein levels, running at 68 and 65 kDa respectively. The *KLHL24-ΔN28* was
20 more abundantly expressed than its wild type counterpart, consistent with results previously reported by Lin et
21 al⁶. Our data are also in line with recent publications showing that loss of function mutations in *KLHL24* are
22 associated with increased desmin expression in myocardial biopsies and a hypertrophic cardiomyopathy
23 phenotype (22, 23). Although our data indicates that *KLHL24* could be detected throughout the cell by IFA, the
24 antibody was not sensitive enough to detect endogenous levels of *KLHL24* in hiPSC-CM or dyn-EHTs, by
25 immunoblot. However, the antibody was sensitive enough to detect exogenous overexpressed *KLHL24*. Similar
26 sensitivity issues had been encountered by He et al., and Lin et al. in patient primary keratinocytes and skin
27 biopsies (4, 5).

28 Desmin expression in heart muscle is low during development and increases only when cardiomyocytes
29 near terminal differentiation (11). Clear compensatory proteins (i.e.: for example nestin, a marker of early
30 cardiac development (24)) are set in place in the early phase of development, which complicates desmin research

1 using relatively immature hiPSC-CMs (25). Cytoskeletal IFs are furthermore believed to be dispensable in 2D
2 monolayer cultures as their specific purpose is to maintain the integrity of 3D tissue structures, which makes
3 current use of 2D cultures rather limited (24). To some degree, our dyn-EHTs model bypassed these limitations
4 by using dynamically loaded more mature cardiomyocytes in a 3D tissue environment, making this a well-suited
5 model for genetic diseases that affect the compliance of the desmin network (i.e. desminopathies) (16).

6 In desminopathies, mitochondrial dysfunction is commonly the first and most prominent defect (10).
7 When complete collapse of the desmin network occurs, nuclear deformations and intercalated discs
8 mislocalizations follow, triggering apoptosis and fibrosis. Notably, in patients and transgenic *DES* animal
9 models, all myopathic *DES* mutations eventually lead to an accumulation of desmin positive aggregates, that
10 contribute to the disease pathology (10, 24). Desmin knockout mice, on the other hand, develop all the
11 aforementioned characteristics, except for the aggregates. They are fertile and develop normally, but all mice
12 eventually develop DCM (26), again prominently due to mitochondrial failure. Furthermore, since these mice
13 lack desmin, they are unable to deform and resist physical stress, leading to intracellular disorganization of
14 organelles. These features are believed to play the most prominent role in the development of DCM (10, 26).

15 There are several overlapping aspects between KLHL24- Δ N28-mediated desmin deficiency and
16 desminopathies. First, tissues showed dilatation upon loading, similar to many desminopathies. Second, TEM
17 revealed swollen-like mitochondria and electron denser glycogen storage vesicles in patient-derived dyn-EHTs.
18 These results were confirmed by Seahorse experiments, which showed that the mitochondrial respiratory
19 function is already impaired in patient hiPSC-CMs in 2D cultures. Third, some potential compensatory
20 mechanisms were observed, like the elevated protein levels of actin and nuclear lamins, indicating that patient-
21 derived dyn-EHTs might be compensating to maintain contractile function and prevent events like nuclear
22 delamination. Several of the desminopathy hallmarks are thus present in our model and show high resemblance
23 to pathogenic human *DES* mutations and the desmin knockout mouse model. However, the KLHL24- Δ N28-
24 induced pathology is also different in two ways. First, the activity of the proteasomal degradation pathways is
25 distinctive. Desmin knockout mice do not express desmin, hence no proteasomal degradation of desmin takes
26 place. In human desminopathies, the accumulating of desmin aggregates severely disrupts cellular protein quality
27 control systems and in turn leads to impaired proteasomal activity. The pathology of KLHL24- Δ N28 is different
28 from both aforementioned, as it displays an overactive proteasomal degradation pathway due to excessive
29 breakdown of desmin. Second, in knockout mice the desmin network is absent while in human disease, desmin
30 aggregates ultimately contribute to collapse of this network (12). In our 3D model the desmin network remained

1 intact (i.e.: both in patient-derived dyn-EHTs as well as in the patient explanted heart), despite 10-fold lower
2 levels of desmin. This likely explains why several common desminopathy hallmarks like nuclear deformations,
3 myofibril abnormalities and intercalated discs mislocalisations were not observed.

4 Our dyn-EHT model shows that the KLHL24-ΔN28-induced tissue dilatation and reduced uniformity,
5 underlies the lower systolic and diastolic forces, higher systolic and diastolic peak stress and non-uniform tissue
6 diastolic stress. Using FEM, patient-derived dyn-EHTs were shown to have a 6-fold increase in peak diastolic
7 cardiomyocyte stress levels compared to controls. On a regional scale, tissue stress and fractional shortening
8 varied widely in patient-derived dyn-EHTs, and a negative correlation was observed between shortening and
9 diameter. In DCM as well as numerous other heart failure etiologies, left ventricular wall stress is frequently
10 increased. Our data indeed closely resembles FEM of human left ventricular myocardial wall stress, that
11 indicated that heart failure patients with reduced ejection fraction had significantly higher average
12 cardiomyocyte stress than controls (27). In our previous research, we also used the dyn-EHTs model, in order to
13 provoke disease in desmoplakin (DSP)-mutated hiPSC-CMs (16). Comparing the two cardio-cutaneous disease
14 models, the etiology is quite different, even though mutations in both genes affect the stretch-bearing structural
15 network of tissues. In DSP-mutated dyn-EHTs, cell-cell contacts were diminished causing dilatation and partial
16 loss of electrical continuity, ultimately reducing the contractile force and stress. In KLHL24 mutated dyn-EHTs,
17 the intracellular compliance network was impaired, which resulted in tissue thinning in addition to dilatation, but
18 the cell-cell contacts were preserved.

19 Further proof of the KLHL24-ΔN28-induced pathology was provided using either *KLHL24* RNAi or
20 direct desmin overexpression. Both rescue models prevented the excessive tissue dilatation and reduced diastolic
21 and systolic force values, in addition to fully alleviating the elevated diastolic, systolic and contractile stress
22 observed after dynamic loading. These results indicate that by restoring desmin expression, tissue stability
23 regained. Whether methionine gain-of-function mutations are causative for DCM in a systemic model remains to
24 be further investigated.

25 KLHL24 targeted antisense oligonucleotide therapy *in vivo* could be an effective treatment that could
26 benefit patient quality of life significantly, whilst remaining within limits not to create hypertrophic
27 cardiomyopathy by losing KLHL24 expression altogether.

1 MATERIAL AND METHODS

2 Cell culture

3 From human skin biopsies, fibroblast were passaged using Trypsin and cultured in regular DMEM containing
4 15% FCS, 1% sodium pyruvate, 1% glutaMAX, 1% P/S, 1% non-essential amino acids. Fibroblasts were
5 cultured and reprogrammed to hiPSCs, by means of nucleofection with three plasmids, pCXLE-hSK, pCXLE-
6 hMLN and pCXLE-hOCT3/4 that were a gift from Shinya Yamanaka (Addgene plasmid #27078, 27079 and
7 27076), according to previously reported papers (28, 29). Each clonal line was karyotyped and maintained by
8 single cell passaging, as previously mentioned (16). From each human source, three lines were maintained and
9 subsequently checked for pluripotency markers SSEA-4 and OCT3/4. hiPSCs lines were differentiated to
10 cardiomyocytes and purified using lactate. Cardiomyocytes were cultured in 2D monolayers or in 3D tissues. All
11 cell cultures were regularly investigated for mycoplasma contaminations.

12 Cardiac tissue culture

13 Cardiomyocytes were used to generate EHTs, subjected to low loading with 130 μm strips vs. high loading with
14 260 μm strips (dyn-EHTs). Day 22 post differentiation initiation, cardiomyocytes were used to generate (dyn-
15 EHTs), as previously described (16). In short, 90% cardiomyocytes were mixed with 10% healthy cardiac
16 fibroblasts obtained from Lonza® in an extracellular matrix gel (Matrigel® and Collagen type I from Corning)
17 into a designated PDMS mold with strip (see graphical abstract). After gelation, medium was added to cover the
18 tissue. Cardiac tissues started contracting after 1 day. Fabricated cardiac tissues were kept constrained in a
19 PDMS mold for 14 days to fully remodel and compact (EHTs). Hereinafter, tissues were pulled out of their
20 constrained mold (dyn-EHTs), and kept in dynamic culture for an additional 14 days. Cardiac tissues maintained
21 spontaneous contractile properties, and responded to electrical pacing. Videos for functional analysis were
22 generated at day 7, day 14, right after confinement, and at day 28, using a Zeiss Axio Zoom V16 microscope
23 connected to a HRm camera and a Nikon SMZ18 microscope connected to a Nikon DS-Qi2 camera. Tissues
24 were terminated and processed at day 28.

25 Cardiac tissue analysis

26 Videos were analyzed according to a custom made MATLAB® code, based on FEM, according to our previous
27 article (16). Additional analysis included, tissue uniformity assessment, regional strain tracking and regional
28 stress mapping. To determine the degree of tissue uniformity induced upon loading, the tissues' smallest cross

1 section area was divided by the largest cross sectional area \emptyset , at time points day 14 (reference) and 28 (after 14
2 days of dynamic loading). These numbers were used to determine whether this number decreased with loading,
3 which is noted as the ratio of tissue uniformity (i.e.: (smallest / largest \emptyset at d28) / (smallest / largest \emptyset at d14)).
4 Regional fractional shortening was quantified using a modification of methods, previously described for speckle
5 tracking in echocardiography (30). Briefly, video frames of peak diastole and systole were isolated. Tissues were
6 divided into three regions, where each region had approximately the same diameter across its longitudinal axis.
7 Six speckles, or noticeable differences in gray values that could be tracked from diastole to systole, were
8 identified in each region. Speckles were tracked using Fiji's Manual Tracking Plugin. Regional fractional
9 shortening (FS) was then calculated (using the equation below) for each pair of speckles, by subtracting the
10 initial distance between each speckle (L_0) from the final distance between each speckle (L_t) and dividing that
11 by the initial distance between each speckle (L_0). This resulted in 15 total measurements per region, which were
12 averaged to get the fractional shortening in that region.

$$FS = \frac{L_t - L_0}{L_0}$$

13 Peak contractile, diastolic and systolic stress calculations were determined based on force values and cross-
14 sectional area, assuming 100% cardiomyocyte content of whole tissue cross-section, determined by the smallest
15 measurable tissue diameter. In our previous method (16), we used 10% cardiomyocyte content for all tissues,
16 based on histology results obtained from both control and DSP-patient-derived dyn-EHTs, that were all uniform.
17 However, KLHL24-patient-derived dyn-EHTs had varying degrees of cardiomyocyte content, therefore no
18 assumptions of actual cardiomyocyte content could be made, without doing histology on each individual tissue
19 section.

20 Regional diastolic stress mapping was performed using finite element analysis with ANSYS Static Structural
21 Software. First, representative tissue geometries were created in ANSYS Space Claim Software from binary
22 images of tissues at diastole. This resulted in a model with accurate thickness displayed from the binary image.
23 Since aerial images were not taken of the tissues, tissues from each group were assumed to have the same
24 thickness in the z-dimension. Material properties were derived from diastolic stress-strain curves using a custom
25 mounted optical force transducer (World Precision Instruments, SI-KG20). These values were fit to a first order
26 Arruda-Boyce hyperelastic model, based on best fit to uniaxial test data. Tissues were uniaxially stretched in

1 ANSYS software using the diastolic force obtained from the PDMS strip analysis. The optimal discretization of
2 elements within the FE mesh used, was determined by slowly decreasing the mesh element size until little
3 change in maximum Equivalent (Von-Mises) Stress was observed between subsequent modeling runs.

4 **Lentiviral transduction and HEK transfection studies**

5 To generate two *KLHL24* knockdown expression patient II:3 hiPSC lines, we combined the envelope (VSV-G)
6 and packaging vector (pCMVΔ8.91) with a *KLHL24*-shRNA transfer pLKO1 vector (Sigma MISSION®
7 shRNA; TRCN0000323203). These lines were compared against two negative control II:3 hiPSC lines, for
8 which we combined the envelope and packaging vectors with a non-targeted-shRNA transfer pLKO1 vector
9 (Sigma MISSION® NT-shRNA;). To generate a *DES* overexpression (oeDES) patient II:3 hiPSC line, we
10 combined the envelope and packaging vectors with a desmin (NM_001927.3) containing pReceiver-Lv156
11 vector (GeneCopoeia™). First, HEK293T cells were transfected using Fugene HD to produce lentiviral particles.
12 Viral particles were collected and hiPSC lines were transduced with addition of polybrene in 6wp at 50%
13 confluence. 48hrs post transduction, successfully transduced hiPSC were selected using puromycin.

14 For exogenous co-expression studies in HEK293A cells, desmin, *CUL3* and *RBX1* were cloned into the
15 pcDNA3.1(+) backbone. Another desmin, *KLHL24*, *KLHL24-ΔN28* and *KLHL24-
16 ΔN28/E355A/E535K/Y584C* [*KLHL24-ΔN28-inactivated*](4) were cloned into the pcDNA3.1(+)-N-DYK
17 backbone. Plasmids were expanded by insertion into viable cell lines, LB-broth culture and midi-prep isolation.
18 HEK293A cells were grown in 12wp until 70% confluency and co-transfected with 500ng of each plasmid in
19 different combinations using Fugene 6. Bortezomib was used to inhibit proteasomal degradation in a
20 concentration of 400 nM for 24hrs. 48hrs post transfection, cells were fixated with methanol:aceton (1:1) and
21 immuno-labeled or proteins and RNA was harvested.

22 **Immunofluorescence analysis**

23 Dyn-EHTs were fixated for 5hrs in 2% formalin, followed by incubation through a tissue transfer processor,
24 finalized by paraffin embedding. Paraffin embedded explanted heart biopsies/ dyn-EHTs were sectioned to
25 histology slices of 5 μm using a microtome. Slices were deparaffinized and rehydrated through xylol/ethanol
26 treatment. Histology slices were then blocked in 3% BSA/PBS for 1hr at RT before incubation with primary
27 antibody (**Table.S1**) in blocking buffer for 1hr at RT or overnight at 4°C. Histology slices were then washed in

1 PBS and incubated with secondary antibody in blocking buffer for 1hr at RT. Histology slices were washed and
2 mounted with DAPI, before imaging.

3 Cultured cells were fixated and immuno-labeled depending on the cell source and antibody (Supplemental Table
4 1). In short, hiPSC were seeded on vitronectin-coated coverslips and fixated for 30 min with 4%
5 paraformaldehyde at RT. Cardiomyocytes were seeded on Geltrex-coated coverslips and either fixated for 10
6 min with methanol:acetone (1:1 at -20°C) or 4% PFA (at 4°C). Formaldehyde-fixated cells were permeabilized
7 with 0,3% Triton for 5 min. Cells were then blocked for 30 min with blocking buffer of 3% BSA/PBS containing
8 2% serum (host of secondary antibody). Cells were then incubated with primary (Supplemental Table 1)
9 antibody in blocking buffer for 1hr at RT or overnight at 4°C. Cells were washed and subsequently incubated
10 with secondary antibody (Alexa 488 and/or 555) in blocking buffer for 1hr at RT. Cells were washed and
11 mounted with mounting media containing DAPI. All slides were imaged using a Leica DMI6000B fluorescent
12 microscope.

13 **Immunoprecipitation**

14 Cardiomyocytes were cultured as monolayers up to day 40 for desmin to become sufficiently expressed. Cells
15 were treated with 10 µM Bortezomib (sigma) for 6hrs before 30 min incubation in lysis buffer (20 mM Tris-HCl,
16 pH 8.0, 1 mM EDTA, 1% NP-40, 10 mM N-Ethylmaleimide and protease inhibitors (Roche 11873580001)) on
17 ice. Lysates were centrifuged 10,000g at 4°C for 10 min and the soluble fraction was used for
18 immunoprecipitation (desmin clone RD301 (IgG2b) and a negative control IgG), using Magnetic Protein G
19 SureBeads (Bio Rad). HEK293A cells were cultured in 60mm dishes and transfected using different
20 combinations of CUL3, RBX1, FLAG-tagged-desmin and KLHL24 plasmids (section above). Cells were treated
21 with 400 nM Bortezomib (sigma) for 24hrs before 30 min incubation in lysis buffer (20 mM Tris-HCl, pH 8.0,
22 1% NP-40, 10 mM N-Ethylmaleimide and protease inhibitors (Roche 11873580001)) on ice. Lysates were
23 centrifuged 10,000g at 4°C for 10 min and the soluble fraction was used for immunoprecipitation (anti-FLAG),
24 using Magnetic Protein G SureBeads (Bio Rad). In short, antibodies (2-20 µg in lysis buffer) were bound to the
25 magnetic beads for 1hr at RT via rotation. Magnetic beads were magnetized and washed 3x with lysis buffer.
26 Protein concentrations in the soluble fraction were measured with the Pierce protein assay. Beads were incubated
27 with soluble protein for 3hrs at 4°C via rotation. Magnetic beads were magnetized and washed 1x with lysis
28 buffer and 2x with PBS-T. Finally, beads were boiled in 1x sample buffer (62 mM Tris-HCl, 2,5% SDS, 1 mM

1 EDTA, 10% glycerol, 5% β -Mercaptoethanol and bromophenol blue) for 10 min at 90°C to elute the lysates.
2 NOTE for cardiomyocytes only: 6hrs of 10 μ M bortezomib treatment was not sufficient to restore desmin levels
3 of patient cardiomyocytes to wild type levels in control cardiomyocytes. Meanwhile, longer incubation periods
4 eliminated their contractile properties and caused too much cell death. Therefore, while maintaining similar
5 protein concentrations in the eluents during immunoprecipitation, we normalized on gel electrophoresis for the
6 amount of precipitated desmin afterwards.

7 **Gel electrophoresis and western blotting**

8 Total protein lysates were extracted from snap frozen dyn-EHTs or cultured cells, using a buffer containing 62
9 mM Tris-HCl, 2,5% SDS and 1 mM EDTA, protease inhibitor (Roche 11873580001), phosphatase inhibitor
10 cocktail 3 (p2850; Sigma) and Sodium orthovanadate. Protein concentrations were measured with the Pierce
11 protein assay. All samples were diluted until 1,5 μ g/ μ l with sample buffer (final solution contains 10% glycerol,
12 5% β -Mercaptoethanol and bromophenol blue). Samples were heated for 5 min at 99°C, with the exception for
13 OXPHOS proteins, of which no heating was applied. Proteins and immunoprecipitated fractions were separated
14 in SDS-PAGE gels and transferred to PVDF or nitrocellulose membranes using tank or semi-dry blotting
15 (depending on the protein size) for 2hrs. Membranes were washed and stained with Ponceau S. Hereinafter,
16 membranes were blocked (polyvinylpyrrolidone(PVP)-based) and incubated with primary (overnight at 4°C)
17 (Supplemental Table 1) and secondary-HRP labeled (1hr at RT) antibodies, before detecting with
18 electrochemiluminescence. For each blot either GAPDH or Vinculin was used as loading control.

19 **RT-PCR**

20 Dyn-EHTs were snap frozen at day 28, prior to RNA isolation. Total RNA from hiPSC, hiPSC-CMs and dyn-
21 EHTs was isolated by phenol-chloroform extraction (TRIzol, Sigma). cDNA was synthesized by reverse
22 transcription and real time qPCRs were performed using SYBR® Green (Sigma; see primer-list in Supplemental
23 Table 2). Relative expression levels were calculated using the 2- $\Delta\Delta$ Ct method.

24 **Transmission electron microscopy**

25 Dyn-EHTs were fixed with 2% glutaraldehyde in 0,1M sodium cacodylate at 4°C. After post-fixation in 1%
26 osmium tetroxide/1,5% potassium ferrocyanide (2hrs at 4°C), tissues were dehydrated using acetone and
27 embedded in EPON epoxy resin. 70nm sections were cut longitudinal and transverse in cell direction and

1 contrasted using 2% uranylacetate in water for 45 minutes followed by Reynolds lead citrate for 1 minute. Full
2 nanotomography scans were generated as described by Sokol et al.(31), shortly: the area of interest is scanned at 2.5 nm
3 pixel resolution using the Zeiss supra 55 EM with Fibics (Canada) ATLAS software.

4 **Seahorse assay**

5 Mitochondrial and glycolysis stress tests were performed on cardiomyocytes derived from II:3 shNT and
6 shKLHL24 hiPSC lines. For each stress test, 7 individual experiments were performed (n=7). Cardiomyocytes
7 were randomly seeded (2D) on pre-coated Agilent XF24 Seahorse Cell Culture Microplates, at a concentration
8 of 100,000 cells/well. For each plate, 3 wells were kept without cells, as background. A stress test was performed
9 7 days after seeding. For the mitochondrial stress test, cells were washed and incubated according to the Agilent
10 manufacturer's instructions for 1hr in a humid incubator without CO₂, prior to testing. During the stress test,
11 wells were injected using the Agilent Extracellular Flux Assay Kit with Oligomycin (1µM final concentration),
12 followed by FCCP (0.5 µM final concentration), and finally by Antimycin A and Rotenone (1µM final
13 concentrations). For the glycolysis stress test, cells were washed and incubated according to the Agilent
14 manufacturer's instructions in medium (pH 7.4), 2hrs in a humid incubator without CO₂, prior to testing. During
15 the stress test, wells were injected using the Agilent Extracellular Flux Assay Kit with Glucose (10mM final
16 concentration), followed by Oligomycin (1µM final concentration), and finally by 2-DG (50mM final
17 concentration). After testing, microplates underwent a freeze-thaw cycle, and protein concentrations were
18 measured using a Biorad protein quantification kit, for normalization.

19 **Statistics**

20 A Shapiro-Wilk normality test was performed on all data sets and sets were subsequently checked for outliers
21 (ROUT Q=1%), prior to analysis. For figure 2 and 3 (and supporting supplemental figures), statistical analysis
22 was based on n=3 control-derived and n=2 patient-derived individuals, supported by 3 hiPSC lines per
23 patient/control and a minimal of n>3 tissues per line. Statistically significant differences between functional
24 tissue parameters were calculated using a 2-way ANOVA, post-hoc Sidak's multiple comparisons test. Non-
25 binned Zeiss videos were used to assess regional fractional shortening. A Brown Forsythe test was used to assess
26 homogeneity of variances. To determine differences in regional fractional shortening based on tissue cross-
27 sectional area, a 2-way ANOVA, post-hoc Sidak's multiple comparisons test was performed. For correlation
28 analysis between regional fractional shortening and tissue diameter, a spearman non-parametric correlation was

1 performed. Statistically significant differences in small-set gene and protein expression levels were calculated
2 using an unpaired *T*-test or Mann-Whitney U test, depending on the outcome of the normality test performed.
3 For figure 4 (and supporting supplemental figures), statistical analysis of protein expression levels in tissues was
4 based on an unpaired *T*-test or Mann-Whitney U test, while a 1-way ANOVA was used for quantifying proteins
5 in HEK-cell transfection studies. For figure 5 (and supporting supplemental figures), statistical analysis were
6 based on adding cardiac tissues derived from the 4 hiPSC lines, treated either with shNT or shKLHL24 mRNA
7 silencing constructs and one hiPSC line treated with a oeDES construct. Statistically significant differences
8 between functional tissues parameters were calculated with a 1-way ANOVA, post-hoc Sidak's multiple
9 comparisons test. Statistically significant differences in protein expression levels were calculated using an
10 unpaired *T*-test or Mann-Whitney U test. Statistically significant differences in large-scale gene expression sets
11 measured in all dyn-EHT groups were calculated using a 2-way ANOVA, corrected for multiple comparisons
12 using FDR via the Benjamini and Hochberg method. For the seahorse assay data, a 2-way ANOVA, post hoc
13 Uncorrected Fishers LSD test was performed. For all statistical tests, a p-value <0.05 was considered significant.
14 Specifics of each statistical test can be found in the figure legends. All statistics were performed using GraphPad
15 Prism. All data is represented as mean ± standard error of the mean (SEM).

16 **Study Approval**

17 This study conforms to the Declaration of Helsinki. Approval of human participants was granted by the medical
18 ethical committee of the University of Groningen (METc 2017/391) and written informed consent was received
19 from all participants. Skin biopsies of family members and controls have been taken at the Dermatology
20 department of the UMCG. The residual fibroblast outgrowth cultures were used to generate hiPSCs, in order to
21 perform this study.

1 AUTHOR CONTRIBUTIONS

- 2 Designing research studies: MCSCV, MCB, HHWS, PvdM
- 3 Establishing methods: MCSCV, JMB, AWF, PHRH, KAG
- 4 Conducting experiments: MCSCV, JMB
- 5 Acquiring data: MCSCV, JMB, DK
- 6 Analyzing data: MCSCV, JMB, MPG
- 7 Writing manuscript: MCSCV
- 8 Critical data interpretation: ALL
- 9 Providing expertise in the field and reagents: MCB, MPvdB, AWF, GFHD, HHWS, BDW
- 10 Collaborators on supported funding: MCB, AWF, PvdM

1 **ACKNOWLEDGEMENTS**

2 We thank Silke Oberdorf-Maass, Frouke Houtsma and Christiane Baierl for their excellent technical
3 contribution. In addition, we would like to acknowledge Annet Linders for contributing additional control-
4 derived dyn-EHT data, Martijn F. Hoes for making additional control hiPSC lines available to this study,
5 Rebecca M. Duffy for establishing part of the dyn-EHT groundwork and Ivan Batalov for writing the
6 MATLAB® code, used for tissue tracking during contraction. Part of the work has been performed at the UMCG
7 Imaging and Microscopy Center (UMIC) and initial videos were shot at ERIBA, department of Laboratory of
8 Stem Cell Regulation and Mechanisms of Regeneration, for which we express our gratitude. This work was
9 supported by the Human Frontier Science Program [grant number RGY 0071/2014 to A.W.F. and P.v.d.M.],
10 Vlinderkind [grant number non-existing; patient organization funding to M.C.B.] and the European Research
11 Counsel [STOP-HF (StG); grant number 715732, ERC-2016-STG to P.v.d.M.]

1 REFERENCES

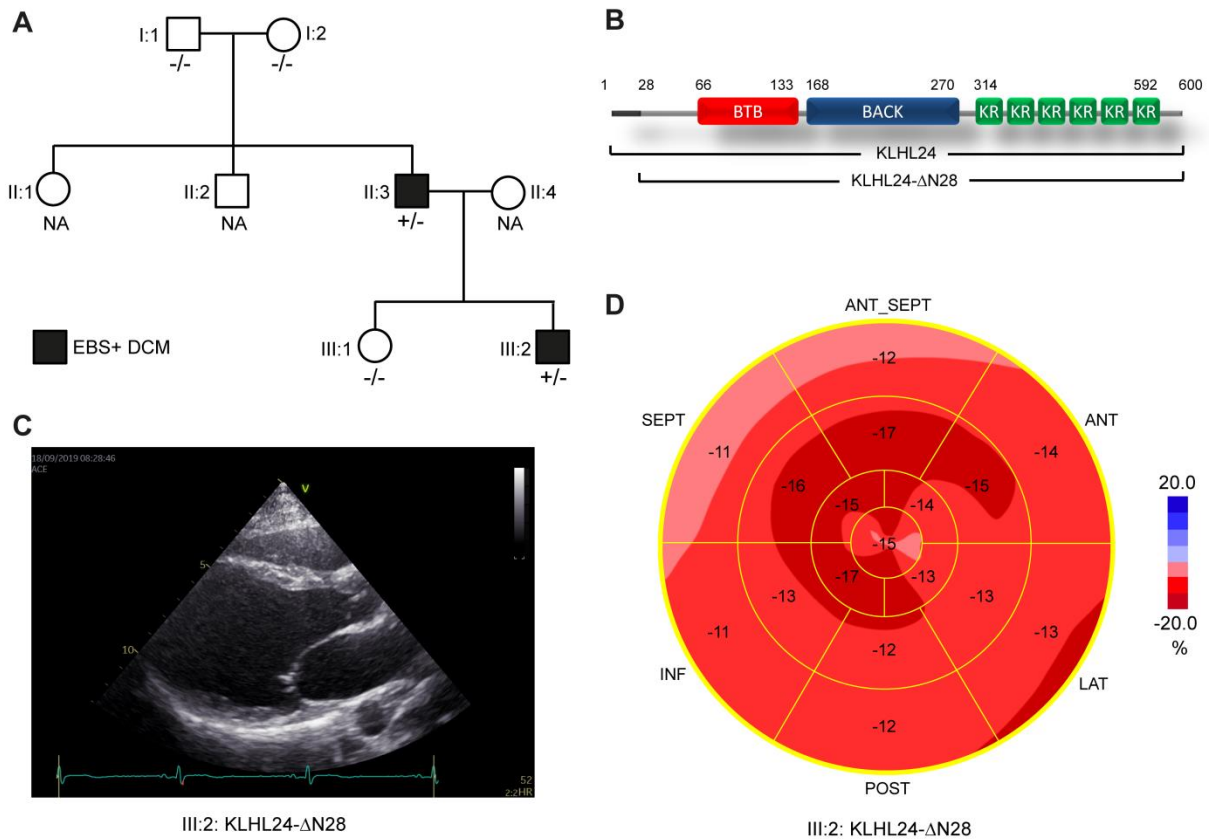
- 2 1. Yenamandra VK et al. Cardiomyopathy in patients with epidermolysis bullosa simplex with mutations in
3 KLHL24. *Br. J. Dermatol.* 2018;179(5):1181–1183.
- 4 2. Schwieger-Briel A et al. Epidermolysis Bullosa Simplex with KLHL24 Mutations Is Associated with Dilated
5 Cardiomyopathy. *J. Invest. Dermatol.* 2019;139(1):244–249.
- 6 3. Grilletta EA. Cardiac transplant for epidermolysis bullosa simplex with KLHL24 mutation–associated
7 cardiomyopathy. *JAAD Case Reports* 2019;5(10):912–914.
- 8 4. Lin Z et al. Stabilizing mutations of KLHL24 ubiquitin ligase cause loss of keratin 14 and human skin
9 fragility. *Nat. Genet.* 2016;48(12):1504–1516.
- 10 5. He Y et al. Monoallelic Mutations in the Translation Initiation Codon of KLHL24 Cause Skin Fragility. *Am. J.*
11 *Hum. Genet.* 2016;99(6):1395–1404.
- 12 6. Alkhalifah A, Chiaverini C, Charlesworth A, Has C, Lacour J-P. Burnlike scars: A sign suggestive of
13 KLHL24-related epidermolysis bullosa simplex. *Pediatr. Dermatol.* 2018;35(3):e193–e195.
- 14 7. Lee JYW et al. Mutations in KLHL24 Add to the Molecular Heterogeneity of Epidermolysis Bullosa Simplex
15 . *J. Invest. Dermatol.* 2017;137(6):1378–1380.
- 16 8. Herrmann H et al. Intermediate filaments : primary determinants of cell architecture and plasticity Find the
17 latest version : Review series Intermediate filaments : primary determinants of cell architecture and plasticity
18 2009;119(7):1772–1783.
- 19 9. Coulombe PA, Kerns ML, Fuchs E. Epidermolysis bullosa simplex: A paradigm for disorders of tissue
20 fragility. *J. Clin. Invest.* 2009;119(7):1784–1793.
- 21 10. Tsikitis M, Galata Z, Mavroidis M, Psarras S, Capetanaki Y. Intermediate filaments in cardiomyopathy.
22 *Biophys. Rev.* 2018;10(4):1007–1031.
- 23 11. Capetanaki Y, Papatheanasiou S, Diokmetzidou A, Vatsellas G, Tsikitis M. Desmin related disease: A matter
24 of cell survival failure. *Curr. Opin. Cell Biol.* 2015;32(February):113–120.
- 25 12. Hnia K, Ramspacher C, Vermot J, Laporte J. Desmin in muscle and associated diseases: beyond the

- 1 structural function. *Cell Tissue Res.* 2015;360(3):591–608.
- 2 13. Milner DJ et al. The absence of desmin leads to cardiomyocyte hypertrophy and cardiac dilation with
3 compromised systolic function. *J. Mol. Cell. Cardiol.* 1999;31(11):2063–2076.
- 4 14. Tse H-F et al. Patient-specific induced-pluripotent stem cells-derived cardiomyocytes recapitulate the
5 pathogenic phenotypes of dilated cardiomyopathy due to a novel DES mutation identified by whole exome
6 sequencing. *Hum. Mol. Genet.* 2013;22(7):1395–1403.
- 7 15. Szeverenyi I et al. The Human Intermediate Filament Database: comprehensive information on a gene family
8 involved in many human diseases. *Hum. Mutat.* 2008;29(3):351–360.
- 9 16. Jacqueline M. Bliley, Mathilde C.S.C.Vermeer, Rebecca M. Duffy, Ivan Batalov, Duco Kramer, Joshua W.
10 Tashman, Daniel J. Shiwarski, Andrew Lee, Alexander S. Teplenin, Linda Volkens, Brian Coffin, Martijn F.
11 Hoes, Anna Kalmykov, Rachele N. Palchesko, Yan S AWF, -. Dynamic Loading of Human Engineered Heart
12 Tissue Enhances Contractile Function and Drives Desmosome-linked Disease Phenotype
13 :<https://www.biorxiv.org/content/10.1101/2020.05.25>.
- 14 17. Agnetti G et al. Desmin modifications associate with amyloid-like oligomers deposition in heart failure.
15 *Cardiovasc. Res.* 2014;102(1):24–34.
- 16 18. Winter DL, Paulin D, Mericskay M, Li Z. Posttranslational modifications of desmin and their implication in
17 biological processes and pathologies. *Histochem. Cell Biol.* 2014;141(1):1–16.
- 18 19. Norgett EE. Recessive mutation in desmoplakin disrupts desmoplakin-intermediate filament interactions and
19 causes dilated cardiomyopathy, woolly hair and keratoderma. *Hum. Mol. Genet.* 2000;9(18):2761–2766.
- 20 20. Protonotarios N, Tsatsopoulou A. Naxos disease and Carvajal syndrome: Cardiocutaneous disorders that
21 highlight the pathogenesis and broaden the spectrum of arrhythmogenic right ventricular cardiomyopathy.
22 *Cardiovasc. Pathol.* 2004;13(4):185–194.
- 23 21. Bolling MC, Jonkman MF. Skin and heart: Une liaison dangereuse. *Exp. Dermatol.* 2009;18(8):658–668.
- 24 22. Hedberg-Oldfors C et al. Cardiomyopathy with lethal arrhythmias associated with inactivation of KLHL24.
25 *Hum. Mol. Genet.* 2019;28(11):1919–1929.

- 1 23. Danielsson O et al. Hypertrophic cardiomyopathy and abnormal glycogen storage in heart and skeletal
2 muscle associated with inactivation of KLHL24. *Neuromuscul. Disord.* 26(2016):S152.
- 3 24. Herrmann H, Strelkov S V., Burkhard P, Aebi U. Intermediate filaments: primary determinants of cell
4 architecture and plasticity. *J. Clin. Invest.* 2009;119(7):1772–1783.
- 5 25. Khudiakov A et al. Generation of iPSC line from desmin-related cardiomyopathy patient carrying splice site
6 mutation of DES gene. *Stem Cell Res.* 2017;24:77–80.
- 7 26. Milner DJ, Weitzer G, Tran D, Bradley A, Capetanaki Y. Disruption of muscle architecture and myocardial
8 degeneration in mice lacking desmin. *J. Cell Biol.* 1996;134(5):1255–1270.
- 9 27. Wang ZJ et al. Left Ventricular Diastolic Myocardial Stiffness and End-Diastolic Myofibre Stress in Human
10 Heart Failure Using Personalised Biomechanical Analysis. *J. Cardiovasc. Transl. Res.* 2018;11(4):346–356.
- 11 28. Okita K et al. A more efficient method to generate integration-free human iPSCs. *Nat. Methods*
12 2011;8(5):409–412.
- 13 29. Takahashi K et al. Induction of Pluripotent Stem Cells from Adult Human Fibroblasts by Defined Factors.
14 *Cell* 2007;131(5):861–872.
- 15 30. Lopez-Candales A, Hernandez-Suarez DF. Strain Imaging Echocardiography: What Imaging Cardiologists
16 Should Know. *Curr. Cardiol. Rev.* 2017;13(2). doi:10.2174/1573403X12666161028122649
- 17 31. Sokol E et al. Large-Scale Electron Microscopy Maps of Patient Skin and Mucosa Provide Insight into
18 Pathogenesis of Blistering Diseases. *J. Invest. Dermatol.* 2015;135(7):1763–1770.

19

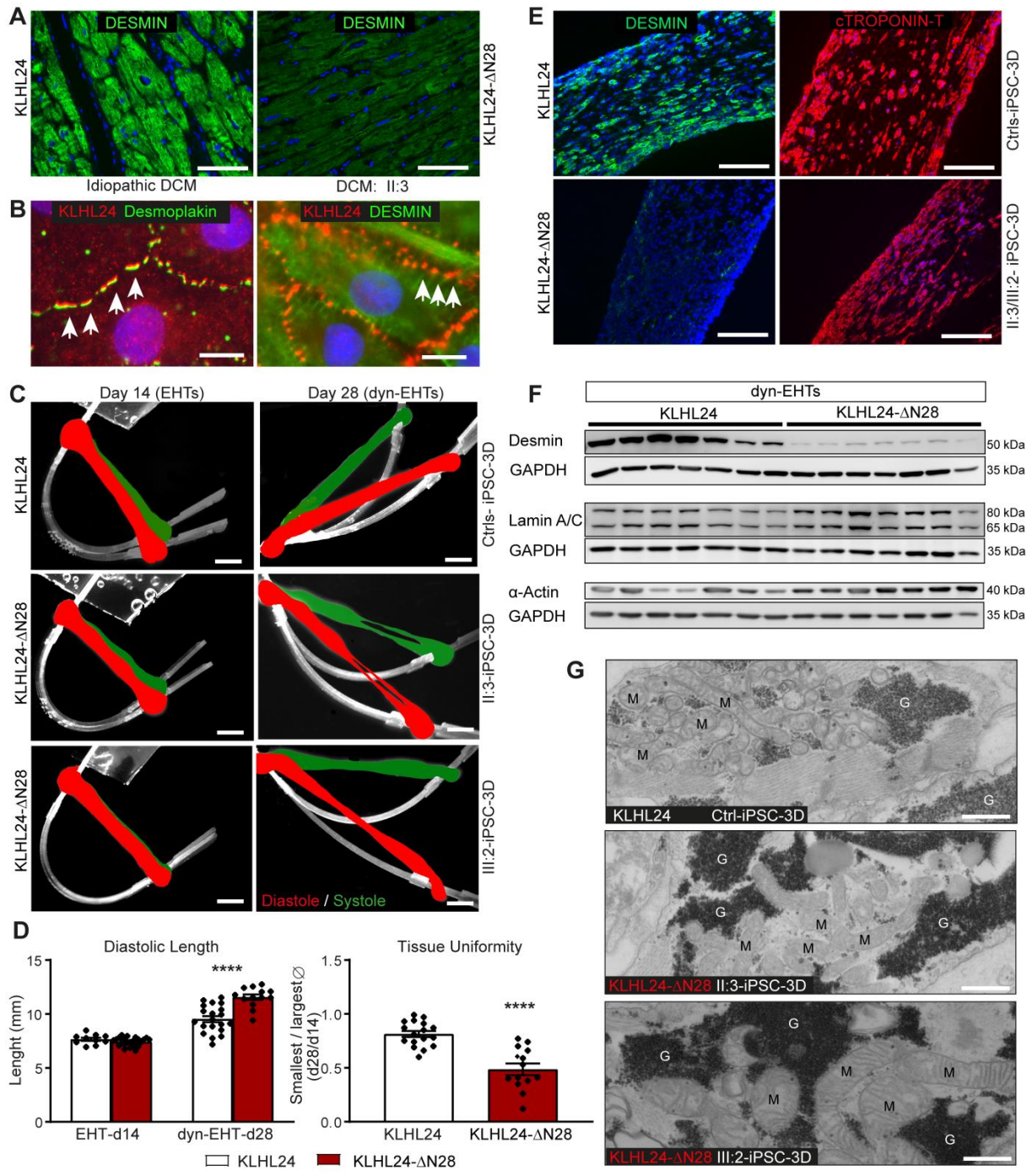
1 FIGURE LEGENDS



2

3 Figure 1: Family tree and clinical characteristics of DCM and EBS.

4 **A)** Family tree showing *KLHL24* genotype-phenotype correlations, where $+/-$ indicates *KLHL24*^{WT/c.1A>G}
5 genotype (heterozygous carrier for mutation c.1A>G in *KLHL24*) and $-/-$ indicates normal *KLHL24*^{WT/WT}
6 genotype. NA indicates unknown genotype. Black box-filled members have an Epidermolysis bullosa simplex
7 and Dilated cardiomyopathy phenotype. **B)** Schematic figure depicting the protein domains of *KLHL24* and the
8 shorter *KLHL24- Δ N28* mutant. BTB=BR-C, ttk and bab; BACK= BTB and C-terminal Kelch; KR=kelch repeat.
9 **C)** Echocardiographic image (long axis parasternal view) of the left ventricle of patient III:2. End-diastolic
10 volume was increased (91 ml/m²; normal value <75) and ejection fraction was reduced (0.51; normal value
11 >0.55). **D)** Bull's eye representation of echocardiographic analysis of different regions of the left ventricle with
12 longitudinal strain imaging (normal value -20%) of patient III:2. Whereas the apex (central part) is relatively
13 spared, in particular the basal regions of the left ventricle (outer ring) show decreased strain values, indicating
14 loss of contractile function. *Note to A) Family tree is updated after our initial observations in 2018 (from*
15 *Yemanandra et al. BJD 2018).*



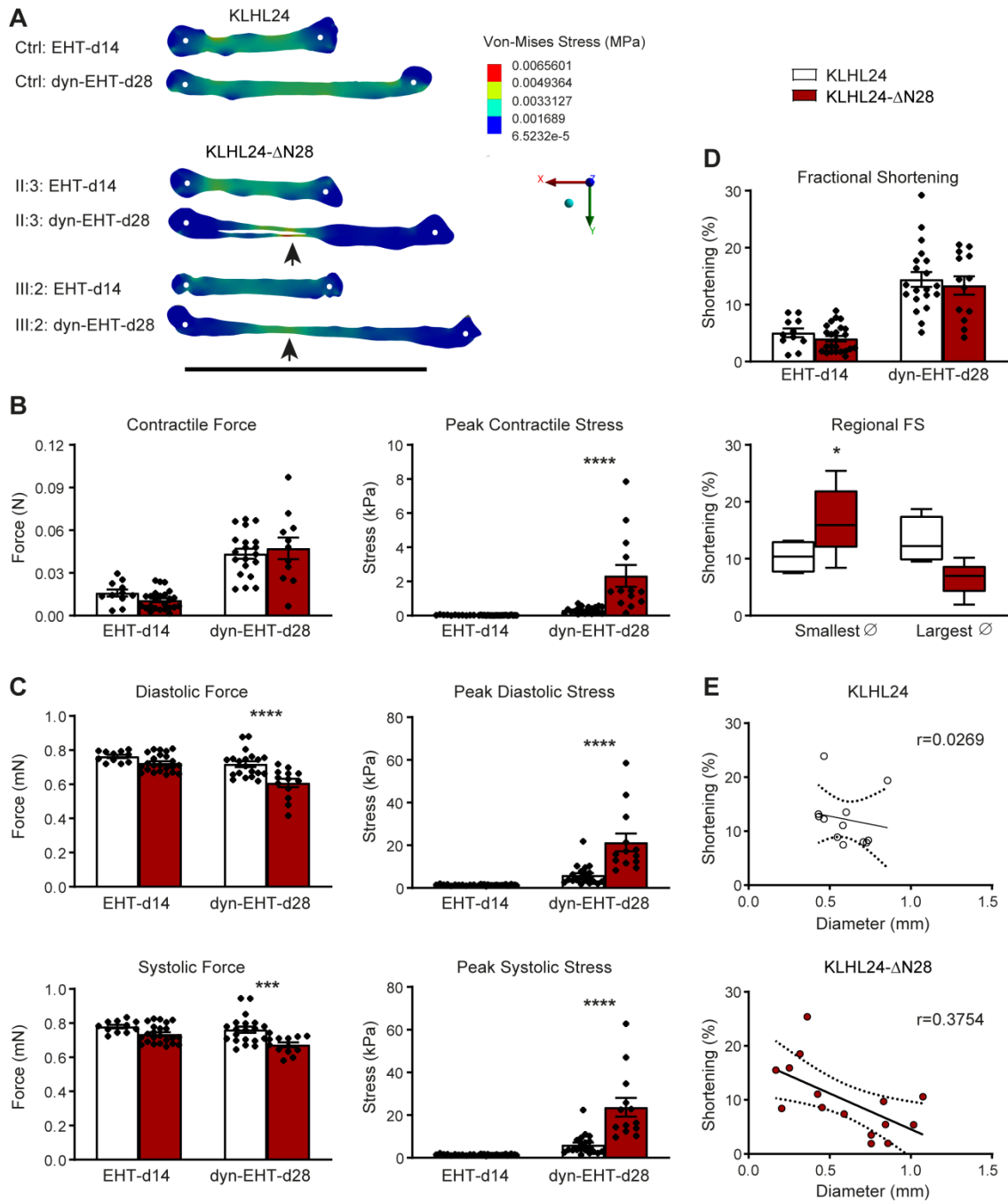
1

2 **Figure 2: Analysis of ex vivo heart and morphology of in vitro patient-derived dyn-EHTs**

3 **A)** IFA labeling of desmin in paraffin sections of the explanted heart of patient II:3 with DCM (KLHL24-ΔN28)
 4 vs. sections of the heart from a patient with idiopathic DCM (named as wild type, KLHL24). Scales bars are 50
 5 μm. Panel A is part of a larger panel depicted in Supplemental Figure 1. **B)** co-IFA of KLHL24 with desmin and
 6 desmoplakin, respectively, in control hiPSC-CMs cultured in 2D. The arrows point to the co-localized areas.
 7 Scale bars are 10 μm. **C)** Side view of contractile EHTs (day 14) right after pulling tissues out of the PDMS

1 molds and after 14 days of dynamic loading dyn-EHTs (day 28). Pictures are representative of all control tissues
2 (KLHL24), derived of three control individuals in the upper panels and both patients in the mid and lower panels
3 (KLHL24-ΔN28). Strips are in white and the images are an overlay of shots taken at diastole (red) and systole
4 (green). Scale bars are 1,5 mm. **D)** Significant differences in morphological parameters between control and
5 patient-derived tissues imaged at day 14 (EHTs) and day 28 (dyn-EHTs). n=11(d14)-20(d28) for controls,
6 n=13(d28)-23(d14) tissues for patients; ****p<0.0001 (Unpaired *T*-test, compared to control dyn-EHTs);
7 ****p<0.0001 (2-way ANOVA, post hoc Sidak's multiple comparison test compared control dyn-EHTs at day
8 28). **E)** IFA labeling of desmin (Y20) and cardiac Troponin T on paraffin sections of control and patient-derived
9 dyn-EHTs at day 28. Images are representative for a n=4 stainings of tissues/group. Scale bars are 200 um. **F)**
10 Western blots depicting affected proteins measured in the three control and two patient-derived dyn-EHTs at day
11 28 (quantified graphs in supplements). **G)** Overview TEM pictures of control and patient-derived dyn-EHTs at
12 day 28, emphasizing the swollen-like mitochondria (M) and electron denser glycogen granules (G) observed
13 throughout patient-derived dyn-EHTs. Scales bars are 75 nm.

1

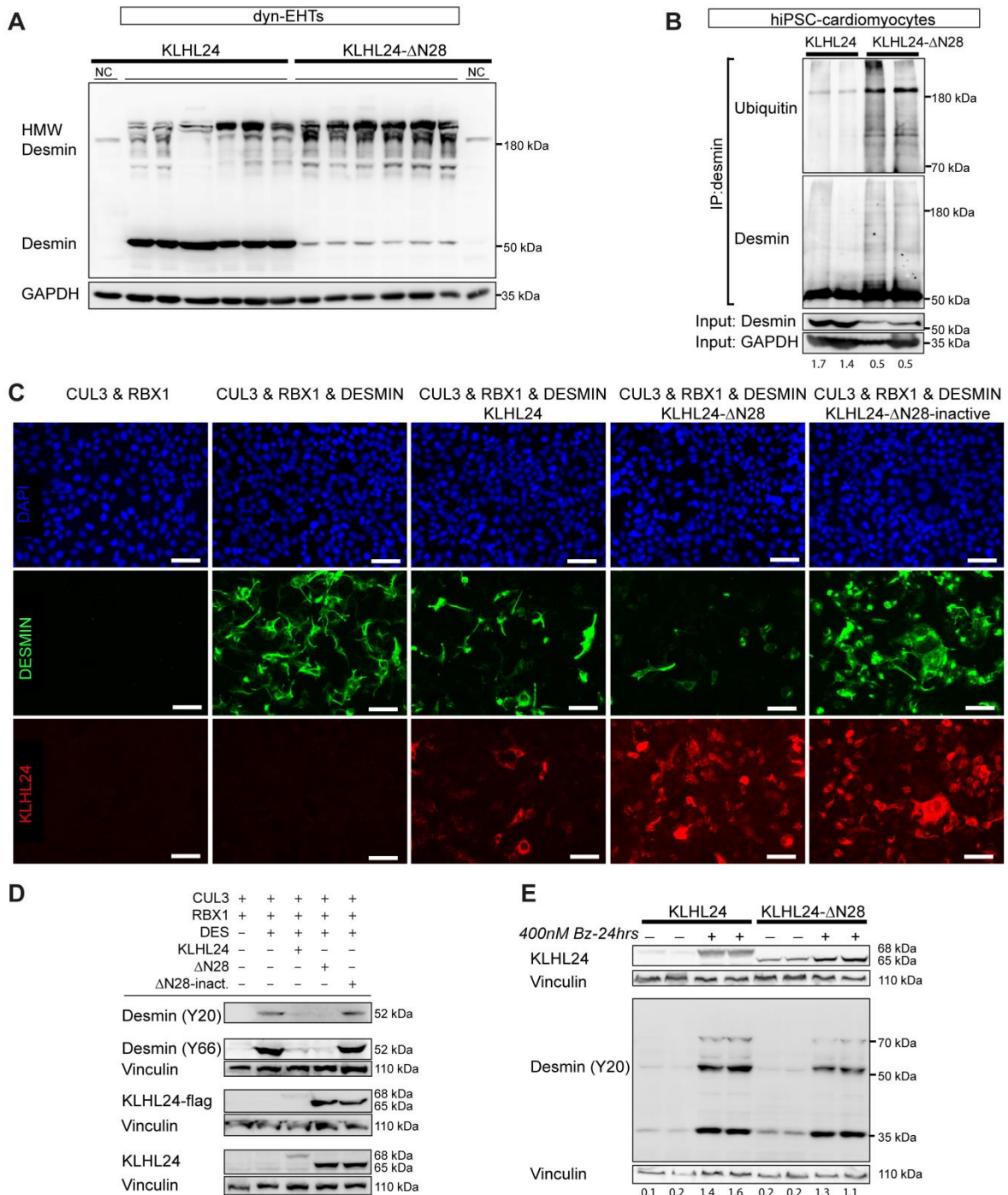


2
3

Figure 3: Functional analysis of patient-derived EHTs/dyn-EHTs

4 **A)** Representative maps of regional diastolic stress, using FEM, in patient and control-derived tissues at the
 5 onset and after 14 days of dynamic loading. Arrows point towards the thinnest sections with the highest stress.
 6 White dots represent the tissue attachment point with the PDMS strip. Scale bar is 10 mm. **B)** Contractile force
 7 and corresponding peak contractile stress of control and patient-derived tissues imaged at day 14 (EHTs) and day
 8 28 (dyn-EHTs). n=11(d14)-20(d28) for controls, n=13(d28)-23(d14) tissues for patients. ****p<0.0001 (2-way

1 ANOVA, post hoc Sidak's multiple comparison test compared to control-derived dyn-EHTs at day 28). **C)**
2 Diastolic and systolic force and corresponding peak diastolic and systolic stress. *** $p < 0.001$ (compared to
3 control-derived dyn-EHTs at day 28); **** $p < 0.0001$ (compared to control-derived dyn-EHTs at day 28). **D)** The
4 average and regional fractional shortening of dyn-EHTs measured as percentages, where speckle tracking
5 analysis is used to determine the latter. * $p < 0.05$ (2-way ANOVA, post hoc Sidak's multiple comparison test
6 comparing smallest diameters of dyn-EHTs at day 28). **E)** Correlation analysis shows a negative correlation
7 between fractional shortening and tissue diameter in patient-derived dyn-EHTs only.

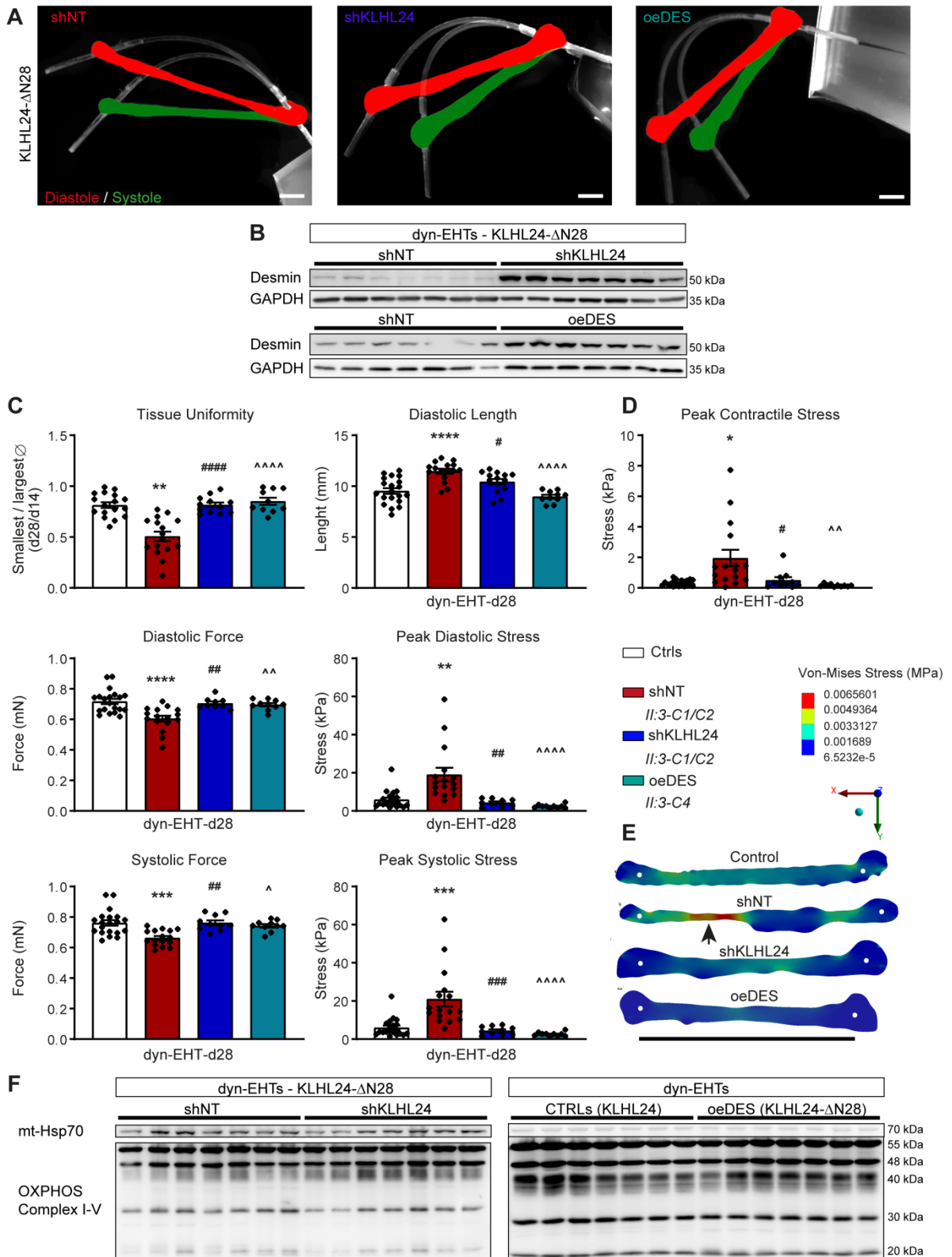


1

2 **Figure 4: Desmin ubiquitination levels in cardiomyocytes and HEK293A transfection studies.**

3 **A)** Western blots depicting the c-terminal-tagged desmin (Y66), showing both the high molecular weight
 4 (HMW) desmin levels as well as the normal (52 kDa) desmin levels in control and patient-derived dyn-EHTs.
 5 NC= negative control; extracts of skin fibroblasts. Quantified levels are in the supplement. **B)** Separate western
 6 blots of desmin (Y66; rabbit) and ubiquitin (FK2; mouse) on different desmin immunoprecipitation fractions (IP
 7 antibody RD301; mouse) of hiPSC-CMs. The input levels used for the IP are depicted below on a separate gel,

1 containing desmin and GAPDH. **C)** IFA staining of desmin and KLHL24 under different combinations of
2 plasmid co-transfections in HEK293A cells (desmin:KLHL24> 1:1 transfection ratio). Scale bars are 25 μ m. **D)**
3 Western blots representative of the same co-transfection set-up depicted in panel C. As all KLHL24 containing
4 plasmids (KLHL24, KLHL24- Δ N28 and KLHL24- Δ N28-inactive) are flag-tagged, blots are depicted of
5 antibodies directed against both flag-tag and KLHL24 protein. Wild type KLHL24 protein runs at 68 kDa,
6 whereas, KLHL24- Δ N28 and inactivated KLHL24- Δ N28 run at 65 kDa. Vinculin poses as loading control. All
7 data are representative of 3 individual transfection experiments. Quantifications are in the supplements. **E)**
8 Western blots depicting the addition of Bortezomib (400 nM Bz) to the co-transfections of CUL3, RBX1 and
9 desmin with either KLHL24 and KLHL24- Δ N28 (desmin:KLHL24> 1:1 transfection ratio). The numbers below
10 depict the ratio of desmin/vinculin.



1

2 **Figure 5: Analysis of patient-derived dyn-EHTs with RNAi of *KLHL24* or desmin overexpression.**

3 **A)** Representative side view pictures of patient-derived shNT, shKLHL24 and oeDES dyn-EHTs at day 28.

4 Strips are in white and the images are overlays of shots at tissue diastole (red) and systole (green). Scale bars are

1 1,5 mm. **B)** Desmin protein levels in shKLHL24 vs. shNT and patient vs. oeDES-derived patient dyn-EHTs,
2 measured on blot (quantified graphs in supplements). **C)** Morphological and functional parameters of patient,
3 shNT, shKLHL24 and oeDES compared to control-derived dyn-EHTs. (n=±15), shKLHL24 (n=15) and oeDES
4 (n=10) patient tissues at day 28 (dyn-EHTs), relative to control (n=20) #p<0.05 (1-way ANOVA, post hoc
5 Sidak's multiple comparison test of patient shKLHL24 vs. shNT dyn-EHTs); ##p<0.01 (patient shKLHL24 vs.
6 shNT); ###p<0.001 (patient shKLHL24 vs. shNT); ####p<0.0001 (patient shKLHL24 vs. shNT); ^p<0.05
7 (patient oeDES vs. shNT); ^^p<0.01 (patient oeDES vs. shNT); ^^p<0.0001 (patient oeDES vs. shNT);
8 **p<0.01 (patient shKLHL24 vs. control). ****p<0.0001 (patient shKLHL24 vs. control). **D)** Peak contractile
9 stress values of above dyn-EHTs. *p<0.05 (1-way ANOVA, post hoc Sidak's multiple comparison test of patient
10 shKLHL24 vs. control); #p<0.05 (patient shKLHL24 vs. shNT); ^p<0.01(patient oeDES vs. shNT). **E)**
11 Representative maps of regional diastolic stress values derived from FEM in patient, shNT, shKLHL24 and
12 oeDES compared to control-derived dyn-EHTs. White dots represent the tissue attachment point with the PDMS
13 strip. Scale bar is 10 mm. **F)** Western blots containing OXPPOS complex proteins (I-V) from patient-derived
14 shNT compared to shKLHL24 dyn-EHTs and patient-derived oeDES compared to control-derived dyn-EHTs.
15 mtHSP70 poses here as a specific loading control. Quantifications are in the supplements.